Contraction-deformation coupling enables the wave-driven morphodynamics and mode-locking of confined active gel droplets

Ryota Sakamoto* and Arash Abedijaberi
Institute of Physics, Academia Sinica, No. 128, Sec. 2, Academia Road, Nangang District, Taipei City 115201, Taiwan, Republic of China

(Received 25 February 2026; accepted 14 October 2026; published 30 October 2026)

Wavelike patterns play fundamental roles in living systems, from single cells to cell collectives, organizing essential functions from wound repair to morphogenesis. While biochemical waves are well established, it remains unclear how the force propagation of cytoskeletal contraction waves regulates cell morphology and migration. Here, we investigate a generic mechanism by which an active droplet exhibits diverse morphodynamics with contraction waves, using a minimal numerical model relevant to living and synthetic cells. We develop a theoretical model in which active gels, representing the active cytoskeleton, generate contraction waves inside a deformable phase-field droplet. The feedback between contraction and deformation organizes cell-like motility modes and revolving contraction waves with unique symmetries. We demonstrate that time-dependent confinement acts as an external driving frequency, entraining contraction waves into a mode-locked revolving state. Our results provide a dynamical-systems perspective on how the coupling of contraction waves and shape deformation of active gel droplets coordinates diverse morphodynamics, a principle relevant to nonequilibrium systems under confinement from living cells to lifelike synthetic cells.

DOI: 10.1103/cnn8-lrdx

I. INTRODUCTION

Wavelike phenomena in living systems play versatile and essential roles in biological function. Wave patterns of biochemical signals guide cell motility and coordinate collective cell organization [1], while directional waves triggered at wound sites orchestrate epithelial and embryonic repair [2,3]. At single-cell level, cytoskeletal reaction-diffusion waves coordinate cell division [4] and adherent cell migration [5] by generating forces and reshaping the actin cortex. These self-organized waves transmit mechanochemical information that governs cell morphodynamics across space and time.

How adherent cell migration is driven by reaction-diffusion waves of biochemical signals, coupled to the force generation of the actin cytoskeleton, has been extensively studied [6,7]. In contrast, nonadherent cell migration [8,9] and the movement of cell-extract droplets [10] are accompanied by "contractile actomyosin waves" [Fig. 1(a)]. Unlike reaction-diffusion waves that propagate toward the cell periphery to generate protrusions [11], contractile waves move backward during cell migration, transmitting nonspecific friction forces to the substrate and propelling the cell body forward [8,10,12,13]. While the actin flow-friction-driven mechanism of migration is well established [13], contractile waves are typically overlooked and approximated as a uniform, averaged flow [8–10]. Thus, how contractile waves contribute to the regulation of cell morphodynamics and migration remains unclear.

To explore the coupling between contractile waves and cell or droplet morphodynamics, theoretical models of deformable interfaces are essential. Recent developments in phase-field models, which describe cells as deformable interfaces, have been widely successful in capturing cellular behaviors accompanied by significant morphological changes. Here, we develop a minimal numerical model of single-cell and cell-extract droplet migration driven by contractile waves. We adopt an active gel theory [14] coupled to phase-field model to investigate how contractile waves drive interfacial morphodynamics. We find that the coupling strength between wave contraction and shape deformation determines the transition from nonmotile to motile states, giving rise to "revolving waves" with unique symmetries. While it has been widely explored that the active gels within phase-field droplets exhibit migratory behaviors [15–25], the distinctive finding in this study is not the droplet motility itself, but the wave-driven revolving morphodynamics and its mode locking under time-dependent confinement. We demonstrate that the waveform of revolving waves is controlled by the geometry and angular velocity of the rotating confinement, providing a dynamical-systems perspective into how wave contraction and shape deformation coordinate under dynamically varying environments.

II. RESULTS

A. Theoretical description of active gels coupled to deformable interfaces

We developed a numerical model of motile active gel droplets driven by contractile waves in a two-dimensional (2D) system. The basic setup includes a confined active gel

*Contact author: rsakamoto@as.edu.tw

Published by the American Physical Society under the terms of the Creative Commons Attribution 4.0 International license. Further distribution of this work must maintain attribution to the author(s) and the published article's title, journal citation, and DOI.

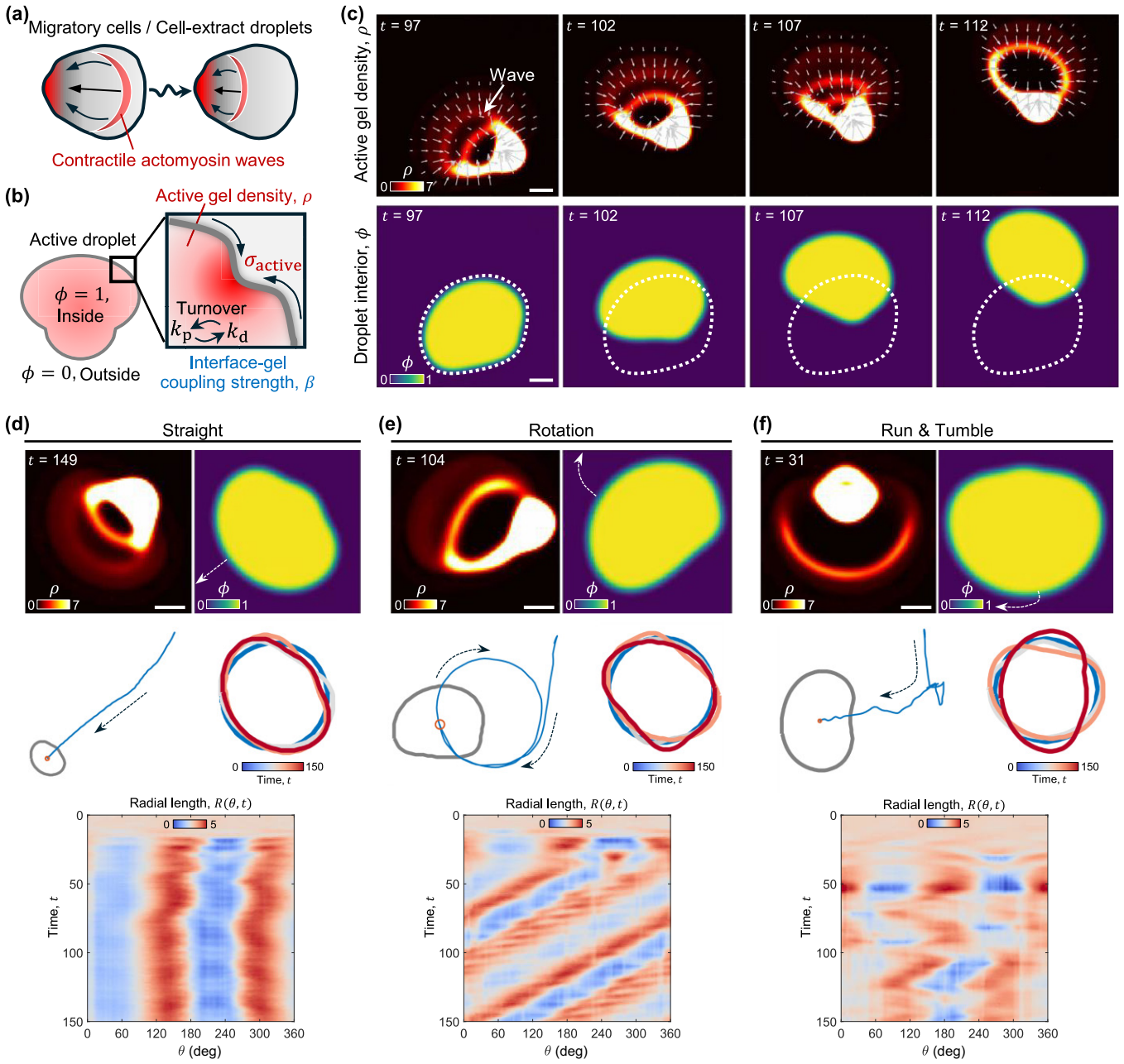


FIG. 1. Active gels coupled to a droplet interface drive contractile wave-driven motility. (a) Schematic of migrating living cells or cell-extract droplets accompanied by contractile actomyosin waves. (b) Theoretical model setup. A phase-field ϕ describes the inside ($\phi = 1$) and outside ($\phi = 0$) of a droplet. The active gel with density ρ undergoing assembly (rate k_p) and disassembly (rate k_d) is confined inside the deformable interface. The gel is interacting to the interface with coupling strength β, and the active stress σ_{active} induces the deformation of the interface. (c) Time-lapse images showing droplet motility induced by the contractive waves of active gels (Movie S1 of the Supplemental Material [38]). The density of active gels ρ (top) and phase-field ϕ describing the droplet interior (bottom) are shown for Pe $= 33$ and $\beta = 43.5$. The gray arrows represent velocity field of the gel. (d)–(f) Various motility modes (Movie S2 of the Supplemental Material [38]). Snapshots showing straight [panel (d), Pe $= 35$ and $\beta = 39$], rotation [panel (e), Pe $= 31$ and $\beta = 43$], and run-and-tumble [panel (f), Pe $= 38.4$, $\beta = 36$, and $R = 4.8$] modes. The density of active gel ρ (left) and phase-field ϕ (right) are shown. The full droplet trajectory is drawn as a blue line with a dashed gray arrow, where droplet outline is drawn in gray, and its centroid is marked as a red circle. Droplet outlines are overlaid at different time points with color code. The bottom kymograph shows time-angle dependence of radial length $R(\theta, t)$ measured from droplet centroids. Scale bars represent 2.

within a phase-field droplet domain [21,26–28] [Fig. 1(b)]. The dynamics of active gels are governed by overdamped force balance and viscous dissipation, which is given by [21,26,29–32]

$$\nabla \cdot (\boldsymbol{\sigma}_{vis} + \boldsymbol{\sigma}_a) = \gamma \mathbf{v}. \quad (1)$$

The force-balance equation (1) includes an active stress $\boldsymbol{\sigma}_a$ generated by the gel, damping from internal viscous stress $\boldsymbol{\sigma}_{vis}$ (see Sec. V for details) and external friction from the cytoplasm and the substrates $-\gamma\mathbf{v}$, where γ is the effective friction coefficient and $\mathbf{v}$ is the velocity of the gel. The mass conservation is given by

$$\frac{\partial\rho}{\partial t} + \nabla\cdot(\rho\mathbf{v}) = D\nabla^2\rho + k_p - k_d\rho, \tag{2}$$

which describes a gel of density ρ that undergoes assembly and disassembly (rates k_p and k_d), diffuses (diffusion constant D), and is advected by the active stress. It is worth noting that the gel density ρ can be interpreted as the density of the actomyosin complex in experimental systems [26,27,32–35]. Starting from two-component mass conservation equations of actin filaments and myosin motors, a single-component mass conservation equation for the actomyosin complex density is derived under the assumption that microscopic myosin binding and unbinding kinetics (on the order of seconds [36,37]) are much faster than cellular-scale actomyosin contraction dynamics (on the order of minutes [8,10]) (Note S1 of the Supplemental Material [38]).

The active gels are confined within a phase-field domain ϕ, representing a spatial confinement such as inside of living cells or cell-extract droplets:

$$\frac{\partial\phi}{\partial t} = D_\phi\nabla^2\phi - \Gamma_\phi V'(\phi) - \beta\mathbf{v}\cdot\nabla\phi. \tag{3}$$

In the phase-field equation [Eq. (3)], D_ϕ describes the effective interfacial tension [21]. The second term with $V'(\phi)$ is the derivative of the double-well potential $V(\phi)$, whose fixed points describe the outside ($\phi = 0$) and inside of the droplet ($\phi = 1$) [Fig. 1(b)] (see Sec. V for details). This term restores the instantaneous droplet volume toward a target volume. The droplet interface has a characteristic width of $(8D_\phi/\Gamma_\phi)^{1/2}$. The last advective term in Eq. (3) represents the interaction between the active gel and the deformable interface. The effective interface-gel interaction is controlled by coupling strength β, which represents contractile [21] or protrusive interaction [16,18] depending on the sign of coupled active gel-induced stresses. Alternative formulations of the interface-gel coupling have been reported in previous studies [28].

The isotropic active stress was assumed to be a function of gel density, $\boldsymbol{\sigma}_a = \zeta f(\rho)\mathbf{I}$, where ζ is the active stress amplitude, $f(\rho)$ is a dimensionless function describing the density dependence, and $\mathbf{I}$ is the identity matrix. We chose the form of density dependence as $f(\rho) = \rho^3/(\rho^3 + \rho_0^3)$, with ρ_0 a constant [21,32]. The thresholdlike nonlinear dependence on gel density was chosen to model the sharp increase in contractility with increasing actomyosin network density (i.e., rigidity percolation [39–41]), as observed during contractile wave generation in cell extracts [10,26,42–44], and in actin flows in migratory blebs [45]. Previous theoretical works describing the actin cytoskeleton used a cubic dependence of active stress on gel density [35,46]. This is reasonable for filament-motor systems [35,46], given that the two filaments and a motor are required to generate contractility, and motor density is expected to be proportional to filament density. We confirmed that such nonlinearity in the density dependence of active stress is essential to induce contractile waves and droplet motility (Fig. S1 of the Supplemental Material [38]). The other choices could be made to describe flow or transient contractile waves [21,26,31,32], which may result in different phase behaviors.

Additionally, it is worth noting that the main physical effect of the thresholdlike dependence of the active stress is to enhance the surface-to-bulk contrast of the active gel, thereby expanding the parameter regime in which ring-shaped waves can form. Our previous work demonstrated that localized gel assembly near the droplet periphery was sufficient to induce a transition from steady flow to ring-shaped wave with a linear density dependence of $f(\rho)$, but only when a sufficiently large ratio of surface-to-bulk gel assembly rate was established, e.g., $k_p^{surf}/k_p^{bulk} > 2.5$ at Pe > 60 [26]. In contrast, incorporating a thresholdlike nonlinear dependence of the active stress promotes gel accumulation near the periphery of a droplet, allowing contractile waves to emerge over a broader parameter range, $k_p^{surf}/k_p^{bulk} > 1$ at Pe > 30 (Figs. S2 and S3 of the Supplemental Material [38]). This robust contractile wave formation makes the present model well suited for investigating wave-driven droplet morphodynamics over a broad region of the phase space.

The full set of equations was nondimensionalized to reduce the parameter space to its essential dimension:

$$\nabla^2\mathbf{v} + \lambda\nabla(\nabla\cdot\mathbf{v}) + \nabla f = \mathbf{v}, \tag{4}$$

$$\frac{\partial\rho}{\partial t} + \mathrm{Pe}\nabla\cdot(\rho\mathbf{v}) = \nabla^2\rho + k_p - k_d\rho + \epsilon_\rho\nabla^2\frac{\delta E}{\delta\rho}, \tag{5}$$

$$\frac{\partial\phi}{\partial t} = D_\phi\nabla^2\phi - \Gamma_\phi V'(\phi) - \beta\mathbf{v}\cdot\nabla\phi. \tag{6}$$

The last term in Eq. (5) is an effective energy to impose an effective no-flux boundary condition to constrain the gel within the droplet as previously introduced [21] (Sec. V). The length and time were normalized by a characteristic length scale $l = (\eta/\gamma)^{1/2}$ and timescale $\tau = \eta/(D\gamma)$. Rescaled parameters were refined as $\rho/\rho_0 \to \rho$, $(k_p\tau)/\rho_0 \to k_p$, and $k_d\tau \to k_d$. The contractility of the gel is effectively controlled by the Péclet number (the ratio of advective transport to diffusion), $\mathrm{Pe} = Ul/D = \zeta/(D\gamma)$, where characteristic active transport speed $U = \zeta/(\eta\gamma)^{1/2}$ was introduced. The constant λ associated with viscosity was assumed to be $\lambda = 1/3$ to simplify the momentum balance equation [21,47] (see Sec. V for details).

To model the localized assembly of cytoskeletal filaments beneath the cell plasma membrane or along the inner surface of cell-extract droplets, the assembly rate k_p near the droplet interface was set to be an order of magnitude larger than in the interior bulk, consistent with previous experimental observations and theoretical models [10,26,43,48] (Sec. V) (Fig. S3 of the Supplemental Material [38]). It should be noted that the enhanced assembly rate near the droplet boundary replenishes gel assembly and provides mass for contractile flows, but does not directly generate a boundary-normal protrusive velocity in contrast to previous works [16,18]. We confirmed that the transition from nonmotile to motile states remains robust across broad variations in the surface-to-bulk assembly rate ratio and the assembly and disassembly rates (Figs. S4–S6 of the Supplemental Material [38]).

It is worth noting that the coupling term $-\beta \mathbf{v} \cdot \nabla \phi$ acts only within the diffuse interface layer of characteristic width $l_{\text{interface}} \sim (D_\phi/\Gamma_\phi)^{1/2}$. Consequently, $l_{\text{interface}}$ and β are not entirely independent, as a broader interface could enhance the effective coupling by extending the region over which this term acts. To assess this effect, we varied the interface width while keeping β fixed. We found that the droplet motility is largely independent of $l_{\text{interface}}$, demonstrating that the observed motile behavior is robust with respect to the diffuse interface width (Fig. S7 of the Supplemental Material [38]). Furthermore, the interfacial width used throughout the main text, $l_{\text{interface}} \approx 0.086$, is approximately one order of magnitude smaller than both the gel correlation length ($l_c = 1$) and the droplet radius ($R = 4.2$), ensuring a clear separation between the interfacial width and the characteristic length scales governing the gel dynamics and droplet geometry.

The set of nondimensionalized equations was numerically solved using semi-implicit spectral methods (Sec. V). In the main text, the effective contractility Pe and coupling strength β were systematically varied to explore their influence on active gel droplet morphodynamics. The other parameters were kept fixed unless otherwise specified, as follows: $k_p = 0.0125$, $k_d = 0.001$, $D_\phi = 8$, $\Gamma_\phi = 1100$, and $\epsilon_\rho = 2$. The initial droplet shape was a circle with radius $R = 4.2$. The initial gel density was set to $\rho = 15$ with small noise (uniform between 0 and 3) if $\phi > 0.99$ and $\rho = 0$ otherwise.

B. Contractile waves drive diverse motility modes

We found that numerical simulations of "active gel droplets" exhibit contractile waves [Fig. 1(c); Movie S1 of the Supplemental Material [38]; Pe = 33 and $\beta = 43.5$], which drive diverse motility modes and dynamic shape changes, including straight, rotational, and run-and-tumble motion [Figs. 1(d)–1(f); Movie S2 of the Supplemental Material [38]]. The motility modes were classified based on the persistence time extracted from the droplet velocity autocorrelation (Fig. S8 of the Supplemental Material [38]). These morphodynamics resemble those observed in migrating cells and cell-extract droplets [8,10], where experiments indicate that actin-membrane interactions play a key role in driving migration [10,49]. To test the impact of interface-gel interaction, the coupling strength β and the effective contractility Pe were systematically varied as key control parameters. Below $\beta \sim 38$, droplets remained circular and exhibited periodic contractions of ring-shaped waves, consistent with previous numerical studies [26] [Fig. 2(a), Movie S3 of the Supplemental Material [38]]. Above $\beta \sim 38$, contractile waves perturbed the droplet position and shape, eventually triggering motility as the droplet broke its symmetrical configuration [Fig. 2(a), Movie S3 of the Supplemental Material [38]].

To quantitatively characterize the nonmotile to motile transition, we analyzed the droplet centroid trajectories over the simulation time course and computed total displacement, d_{tot}, in a Pe–β phase diagram [Fig. 2(b)]. Notably, the total displacement exhibits a jump from $d_{\text{tot}} \simeq 20$ to $d_{\text{tot}} \simeq 40$ by increasing the coupling strength β. In the following analysis, we classify droplets with total displacement $d_{\text{tot}} < 30$ as nonmotile and those with $d_{\text{tot}} > 30$ as motile. Mean-square displacement (MSD) of the long-term droplet trajectory exhibits a clear difference in which motile droplets are ballistic (MSD $\propto \Delta t^2$), while nonmotile droplets are diffusive (MSD $\propto \Delta t$) due to shape changes caused by periodic wave contractions [Fig. 2(c); data along the phase boundary are shown]. The representative motility modes of straight, rotational, and run-and-tumble motion [Figs. 1(d)–1(f)] correspond to ballistic, confined, and persistent random walk dynamics, respectively, as characterized by MSD (Fig. S9 of the Supplemental Material [38]). Ballistic motility has previously been observed in cell-extract droplets [10]. Persistent random walk motion is characterized by short-time ballistic and long-time diffusive dynamics and has been widely reported for nonadherent cells exhibiting contractile actomyosin waves under confinement [8,50].

We verified the phase diagram at lower effective contractility (Pe < 30), where we identified the contractility-dependent transition from nonmotile to motile states, consistent with previous numerical models incorporating actomyosin flow [21] (Fig. S10 of the Supplemental Material [38]). Since our study focuses on how interface-gel coupling strength impacts motility transition, we examine sufficiently high Pe values to ensure robust motile behavior and avoid complexities arising from Pe-dependent transitions. We confirmed that increasing droplet size resulted in the transition from nonmotile to motile state when effective contractility Pe was fixed (Fig. S11 of the Supplemental Material [38]), consistent with previous numerical models [21].

C. Polarized active gels are coupled to shape deformation and persistent motility

Strong interfacial coupling of active gels triggers droplet motility, but how does that influence droplet morphology? To quantify dynamic shape changes, we analyzed the contour shape of droplets [Fig. 2(d)]. Contour position was extracted from the phase field (Sec. V). We then computed the radial length $R(\theta, t)$ and the amplitude of deformation $u(\theta, t) = R(\theta, t) - \langle R(\theta, t)\rangle_\theta$ in polar coordinates centered at droplet centroid, where $\langle R(\theta, t)\rangle_\theta$ is the mean radius averaged over θ at time t. The time-angle kymograph of amplitude at weak coupling strength exhibits a small fluctuation [Fig. 2(e); $\beta = 30$ and Pe = 36], while that of strong coupling strength exhibits a large stable amplitude over time [Fig. 2(f); $\beta = 43.5$ and Pe = 36]. Notably, equal-angle autocorrelation of the deformation amplitude, $C_{\theta\theta}(\Delta t) = \langle u(\theta, t)u(\theta, t + \Delta t)\rangle_{\theta,t}/\langle u(\theta, t)^2\rangle_{\theta,t}$, exhibits a long-tail correlation for motile droplets, reflecting their stabilized deformation, while that of nonmotile droplets rapidly drops to zero [Fig. 2(g)]. The time-averaged aspect ratio of the droplet shape, $\langle \alpha \rangle_t$, significantly increases from $\langle \alpha \rangle_t \sim 1.1$ to $\langle \alpha \rangle_t \sim 1.4$ by increasing the coupling strength β (Sec. V) (Fig. S12 of the Supplemental Material [38]), consistent with the symmetry breaking of droplet shape upon nonmotile to motile transitions in other active droplet models [21,51]. Together, these results suggest that stabilizing the deformed droplet shape is a key requirement for sustaining droplet motility.

To understand how motility and shape changes are stabilized by active gels, we analyzed the polarity P, defined as the normalized center of mass of active gel

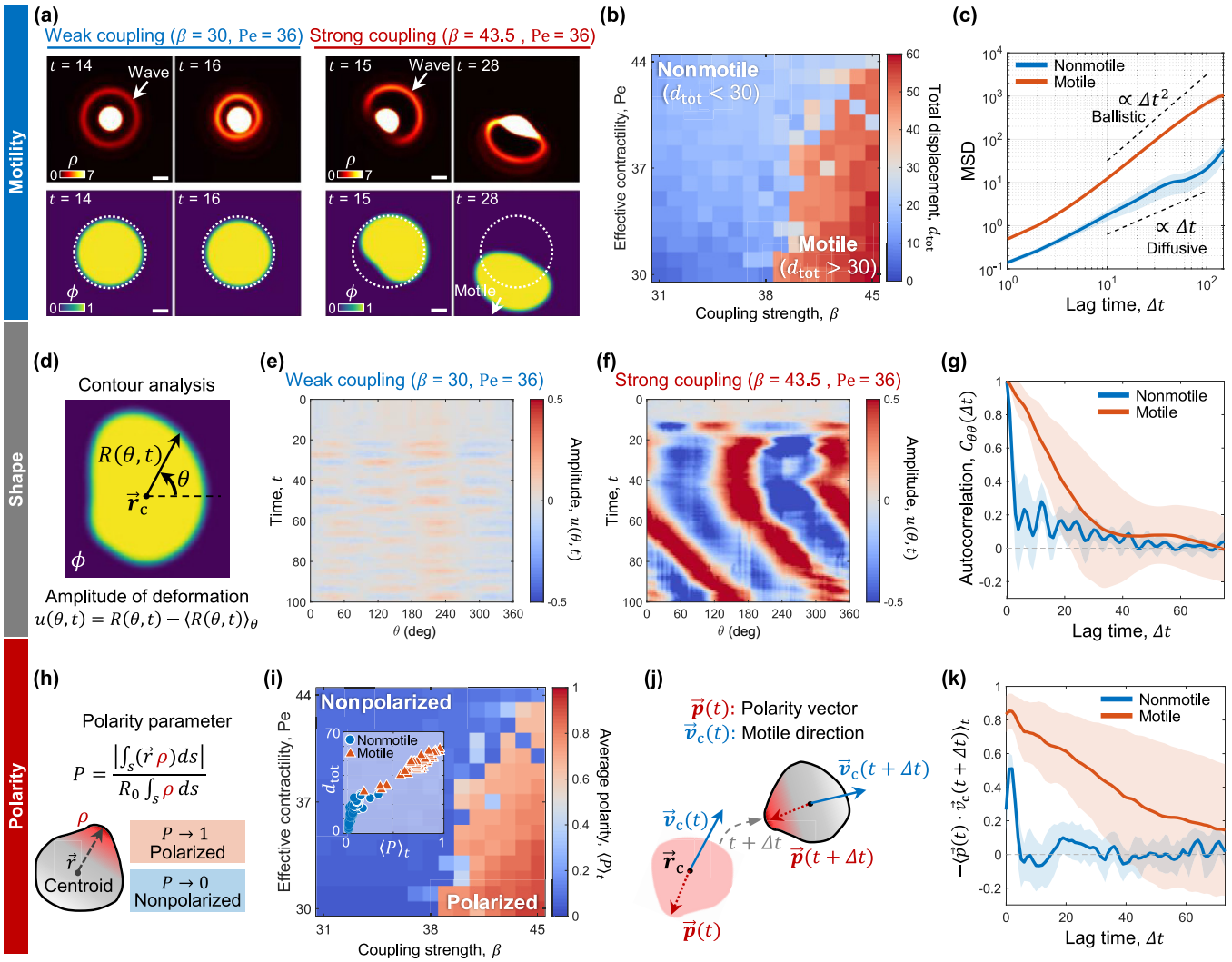


FIG. 2. Droplet motility is coupled to stable shape deformation and polarized gel distribution. Quantitative characterization of motility [panels (a)–(c)], shape [panels (d)–(g)], and polarity [panels (h)–(k)]. (a) Time-lapse images showing a nonmotile droplet under weak coupling strength for Pe = 36, $\beta = 30$ (left), and a motile droplet under strong coupling strength for Pe = 36, $\beta = 43.5$ (right) (Movie S3 of the Supplemental Material [38]). The density of active gels ρ (top) and phase-field ϕ describing the droplet interior (bottom) are shown. (b) Pe–β phase diagram with color-coded total displacement, d_{tot}. We classified motile and nonmotile droplets with the criteria: motile for $d_{\text{tot}} > 30$ and nonmotile for $d_{\text{tot}} < 30$. (c) Mean-square displacement over lag time Δt ($n = 10$ in motile; $n = 11$ in nonmotile). The data points were extracted in the vicinity of the phase boundary. The dashed lines are eye guides for MSD $\propto \Delta t^2$ for ballistic motion and MSD $\propto \Delta t$ for diffusive motion. Curves are mean ± SEM. (d) Contour shape analysis. The distance from the centroid, $R(\theta, t)$, was used to calculate the amplitude, $u(\theta, t) = R(\theta, t) - \langle R(\theta, t)\rangle_\theta$, where $\langle\cdot\rangle_\theta$ denotes the average over angle θ. (e) Time–θ kymograph of the amplitude at weak coupling strength for Pe = 36 and $\beta = 30$. (f) Time–θ kymograph of the amplitude at strong coupling strength for Pe = 36 and $\beta = 43.5$. (g) Equal angle autocorrelation of amplitude over lag time ($n = 10$ in motile; $n = 11$ in nonmotile). Curves are mean ± SD. (h) Schematic showing the definition of polarity parameter P. The polarity parameter approaches 1 for polarized and 0 for nonpolarized gel distribution. The integral is taken along the droplet contour s. (i) Pe–β phase diagram with color-coded polarity averaged over time, $\langle P\rangle_t$. Inset: Scatter plot showing average polarity vs total displacement ($n = 70$ in motile; $n = 155$ in nonmotile). Each point corresponds to different set of Pe and β in the phase diagrams (b) and (i). (j) Schematic showing the definition of instantaneous polarity vector $\vec{p}(t)$ and motile direction $\vec{v}_c(t)$. (k) Cross-correlation of polarity vector and motile direction over lag time Δt ($n = 10$ in motile; $n = 11$ in nonmotile). The minus sign is applied since the polarity and velocity are defined in opposite directions. Curves are mean ± SD. Scale bars represent 2.

distribution near droplet interface: $P = \frac{|\int_s \vec{r}\rho\, \mathrm{d}s|}{(R_0 \int_s \rho\, \mathrm{d}s)}$, where $\vec{r}$ is the contour position, R_0 is the initial droplet radius, and the integral is taken along the contour length s [Fig. 2(h)] (Sec. V). The polarity quantifies the extent of polarized distribution of the gels, where $P \to 1$ and $P \to 0$ represent polarized and nonpolarized gel distributions, respectively. The polarity averaged over time, $\langle P\rangle_t$, exhibits a jump from $P \sim 0$ to $P \sim 0.8$ by increasing the coupling strength β [Fig. 2(i); Fig. S12 of the Supplemental Material [38]], consistent with the trends observed in the total displacement. Indeed, the scatter plot for average polarity $\langle P\rangle_t$ versus total displacement d_{tot} exhibits a positive correlation [Fig. 2(i), inset].

To gain insights into how polarized gels stabilize motile direction over time, we analyzed the cross-correlation between polarity vector $\vec{p}(t)$ and the motile direction of the droplet centroid $\vec{v}_c(t)$ at each time point [Fig. 2(j)]. Notably, the cross-correlation between polarity and motile direction $\langle \vec{p}(t) \cdot \vec{v}_c(t+\Delta t) \rangle_t$ exhibits a large correlation in motile droplets, indicating that the gel polarization is strongly coupled to the motile direction [Fig. 2(k)]. The polarity autocorrelation $\langle \vec{p}(t) \cdot \vec{p}(t+\Delta t) \rangle_t$ exhibits a long-tail correlation, reflecting the stabilized polarity in motile droplets (Fig. S12 of the Supplemental Material [38]). A similar coupling between motile direction and polarity has been reported in cell-extract droplets [10], while a coupling of motile direction and speed has been reported in adherent living cells [52]. These results demonstrate that stabilized gel polarity is essential for persistent droplet motility.

D. Linear stability analysis of coupled phase-field and active gel dynamics

To quantitatively examine the mechanism underlying the motility transition in our coupled system, we calculate the growth rate (ω) of fluctuations around the symmetric base state using an approximate representation of the one-dimensional symmetric steady-state solution, $X_0 = [\phi_0(x), \rho_0(x)]$, while retaining the full linear coupling between the phase-field and active gel, together with the corresponding hydrodynamics (see Note S2 of the Supplemental Material [38] for details) [21]. Our analysis identified an instability controlled by the coupling strength β (Fig. S13 of the Supplemental Material [38]). At sufficiently large β, the leading eigenmodes acquire a nonzero imaginary component, $\mathrm{Im}(\omega) \neq 0$, indicating the emergence of oscillatory dynamics. Near $\beta \approx 36$, the leading eigenmodes become unstable with $\mathrm{Re}(\omega) > 0$, with the most unstable eigenmode becoming predominantly odd in its spatial structure. The resulting odd mode provides a symmetry-breaking perturbation consistent with the onset of polarized active gel distribution and persistent motility observed in the 2D simulations (Fig. S13 of the Supplemental Material [38]). Thus, our results reveal an instability arising from advective feedback between the phase-field and active gels, characterized by interface localization, oscillatory dynamics, and symmetry-breaking perturbations at the onset of motility.

It should be noted that the droplet motility modes observed in the present study are broadly consistent with previous theoretical studies of cell migration and active droplets [15–25]. Our objective, however, is not to investigate the details of migration modes, since oscillatory, rotating, and persistent motions have already been extensively documented in previous works. Rather, we hereafter focus on the active gel dynamics inside deformable interfaces, and on how interfacial deformation feeds back to drive the self-organization of active gels.

E. Revolving waves with specific modes emerge at the phase boundary

Remarkably, we found "revolving contraction waves" near the phase boundary of nonmotile to motile transition [Figs. 3(a)–3(d)]. The revolving waves exhibit characteristic rotational symmetries: a wave with one pole [monopolar wave; Fig. 3(a); Movie S4 of the Supplemental Material [38]], two poles extending from the opposite ends [bipolar wave; Fig. 3(b); Movie S5 of the Supplemental Material [38]], or three poles extending by separating 120° [tripolar wave; Fig. 3(c); Movie S6 of the Supplemental Material [38]]. The droplet shape approximately reflects the rotational symmetry of revolving waves, indicating a mode coupling between the wave contraction and the shape deformation. The revolving waves often transiently emerge, eventually triggering droplet motility (Movie S7 of the Supplemental Material [38]). The emergence of revolving waves highlights a unique role of the deformable interface, which not only responds passively to the enclosed active gel but also guides its dynamics through contraction-deformation coupling. These results together demonstrate the importance of wave-driven contraction-deformation coupling to organize diverse morphodynamics of active gel droplets [Fig. 3(d)].

F. Controlling the modes of revolving waves through rotating confinement

To gain further insights into the mechanism of revolving mode selection, we designed a numerical experiment imposing dynamic deformations on active gel droplets using a potential field (Sec. V). Based on the observations at the phase boundary, we implemented characteristic geometrical confinements for the droplets, including a circle, ellipse, triangle, and square, which were rotated at an angular velocity ω_{rot} (deg/frame) [Fig. 4(a)]. Strikingly, confinement-dependent revolving modes emerged, including quadrupolar waves that were not observed in unconfined droplets [Fig. 4(b); Movie S8 of the Supplemental Material [38]]. It is noteworthy that revolving waves emerged at a specific angular velocity, reflecting the coupling between the timescales of periodic contraction and droplet shape deformation [Fig. 4(c); $\omega_{\mathrm{rot}} = 28$ for bipolar waves; Movies S9–S12 of the Supplemental Material [38]].

To identify the characteristic angular velocity at which revolving waves emerge, we analyzed the equal-time angular correlation of gel shape deformation amplitude, $C_{tt}(\Delta\theta) = \langle u_{\mathrm{gel}}(\theta,t) u_{\mathrm{gel}}(\theta+\Delta\theta,t) \rangle_{\theta,t} / \langle u_{\mathrm{gel}}(\theta,t)^2 \rangle_{\theta,t}$ (Sec. V) (Fig. S14 of the Supplemental Material [38]). The maximum value of the shape correlation, $C_{tt}^{\max}$, measures the extent to which the gel retains specific shape, showing that each revolving wave mode emerges around a certain angular velocity [Fig. 4(d)]. As the wave number increases, the peak angular velocity decreases. This trend is explained by the intrinsic wave period in a droplet without confinement, where it takes time $T_0 \simeq 5.3$ to periodically generate ring-shaped waves (Fig. S15 of the Supplemental Material [38]). For the bipolar wave as an example, it takes twice longer time, $T_{\mathrm{bipolar}} = 2T_0$, to generate the two stable waves simultaneously, given the same contractility and gel assembly rates. Thus, the frequency of bipolar wave is $\omega_{\mathrm{bipolar}} = 2\pi/T_{\mathrm{bipolar}} \times (180/\pi) \simeq 34$, comparable to the peak angular velocity $\omega_{\mathrm{rot}}^{\mathrm{peak}} \simeq 28$ for the bipolar wave. This is applicable to the other revolving wave modes, showing a trend similar to that of the peak angular velocities: monopolar, $\omega_{\mathrm{mono}} = 2\pi/T_0 \simeq 68$ ($\omega_{\mathrm{rot}}^{\mathrm{peak}} \simeq 40$); tripolar, $\omega_{\mathrm{tri}} = 2\pi/(3T_0) \simeq 23$ ($\omega_{\mathrm{rot}}^{\mathrm{peak}} \simeq 20$); and quadrupolar, $\omega_{\mathrm{quad}} = 2\pi/(4T_0) \simeq 17$ ($\omega_{\mathrm{rot}}^{\mathrm{peak}} \simeq 16$).

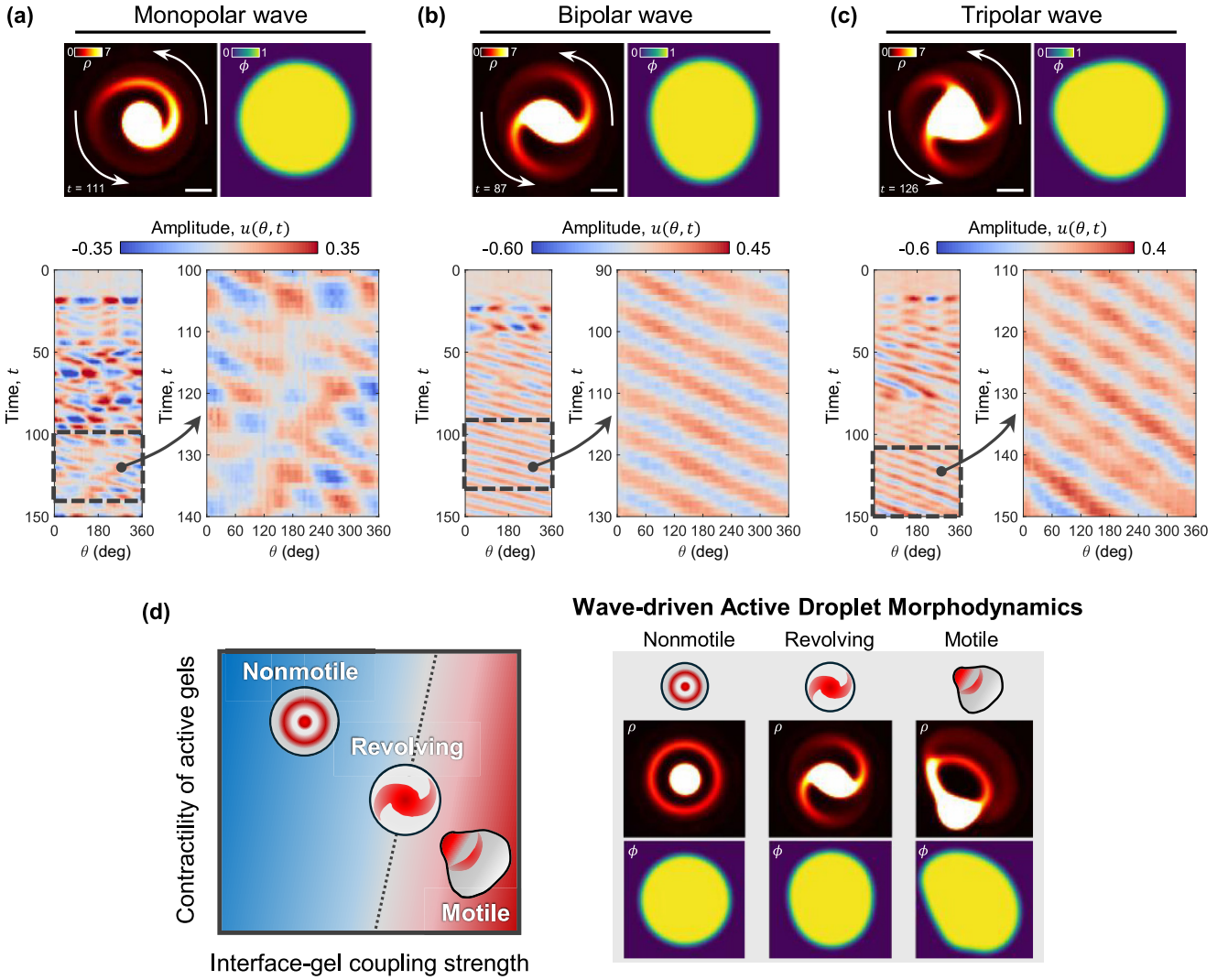


FIG. 3. Revolving waves with rotationally symmetric modes emerge at the phase boundary. (a) Snapshot showing monopolar waves for Pe = 43 and $\beta = 40$ (Movie S4 of the Supplemental Material [38]). The left is active gel density ρ, and the right is corresponding phase-field ϕ. White arrows indicate the direction of revolving. The corresponding time $-\theta$ kymograph of the amplitude of droplet shape deformation is shown. (b) Snapshot showing bipolar waves for Pe = 37 and $\beta = 37$ (Movie S5 of the Supplemental Material [38]). The left is active gel density ρ, and the right is corresponding phase-field ϕ. The corresponding time–θ kymograph of the amplitude of droplet shape deformation is shown. (c) Snapshot showing tripolar waves for Pe = 33 and $\beta = 37$ (Movie S6 of the Supplemental Material [38]). The left is active gel density ρ, and the right is corresponding phase-field ϕ. The corresponding time–θ kymograph of the amplitude of droplet shape deformation is shown. (d) Schematic summarizing the wave-driven morphodynamics of active gel droplets. Nonmotile to motile transition is controlled by the interfacial-gel coupling strength, where revolving waves emerge at the phase boundary as transient states (left). Each phase is characterized by the unique morphodynamics of the contractile waves and the droplet shape (right). Scale bars represent 2.

This result suggests that a mode-locked oscillatory state emerges under rotational geometric confinement. The mode-locked nature is supported by three characteristic behaviors: (1) the wave number (mode) is determined by the corresponding geometric mode of the confinement; (2) each wave mode spontaneously emerges at its characteristic frequency; and (3) wave modes whose characteristic frequencies do not match the rotational frequency of the confinement are suppressed or entrained by the imposed rotation. Consequently, a specific wave mode persists only when its characteristic frequency matches the rotational frequency of the confinement, resulting in the emergence of distinct wave modes only near their corresponding rotational frequencies [Fig. 4(d)]. Together, these results indicate that time-dependent confinement acts as an external periodic drive that reshapes the dynamics of revolving contraction waves, giving rise to mode-locked oscillatory states through temporal coupling between wave contraction and droplet-shape deformation.

G. Revolving wave velocity is determined by a balance between gel assembly and force generation

To better understand how the dynamical feedback between the force generation and assembly of active gels

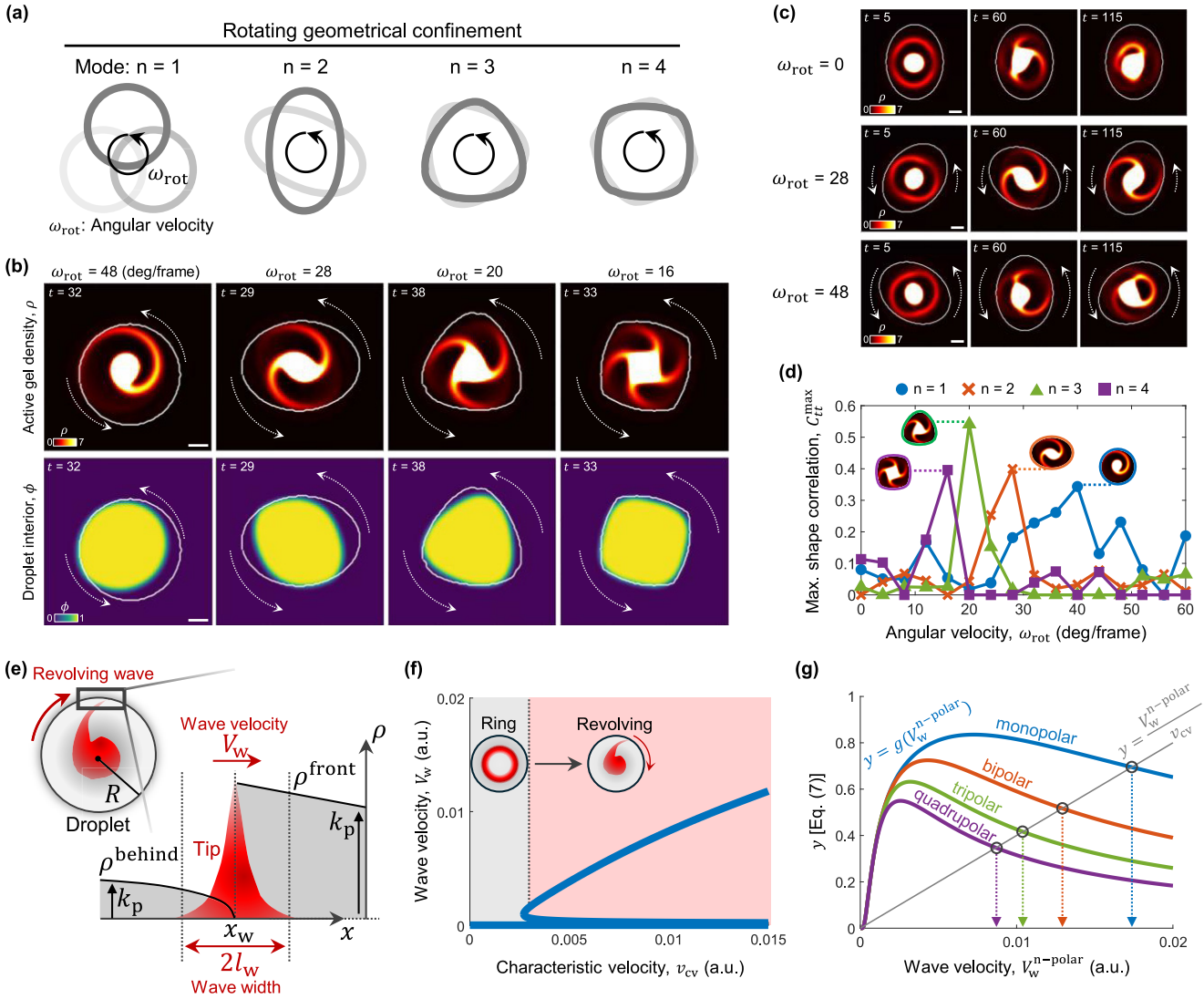


FIG. 4. Controlling the mode of revolving waves using rotating confinement. (a) Schematic showing confinement geometry with different modes. Mode $n = 1$ is a circle with off-centered rotation with angular velocity ω_{rot}; the other modes are rotating around centroids, in which $n = 2$ is an ellipse, $n = 3$ is a triangle, and $n = 4$ is a square. Rotated shapes are shown in transparent light gray. (b) Revolving waves with distinct modes under different confinement modes (Movie S8 of the Supplemental Material [38]). The top is active gel density ρ, and the bottom is corresponding phase-field ϕ. White outlines represent confinement boundary, and white arrows indicate the direction of confinement rotation. (c) Time-lapse images showing active gel dynamics inside a rotating confinement in mode $n = 2$ at different angular velocity ω_{rot} (Movie S10 of the Supplemental Material [38]). (d) Maximum shape correlation C_{tt}^{max} at varied angular velocity ω_{rot} (Movies S9–S12 of the Supplemental Material [38]). The peaks correspond to the angular velocity at which a specific revolving wave mode emerges. The effective contractility and interface-gel coupling strength were fixed at Pe = 37 and $\beta = 39$ for all data. (e) Schematic showing the one-dimensional model of revolving wave motion. A monopolar revolving wave is shown in red. The tip region is magnified and drawn in one dimension along the horizontal x axis and the vertical gel density ρ axis. The wave has a width $2l_w$ and its center-of-mass position is x_w. The wave travels at a constant speed V_w over the periodic domain, $0 < x < 2\pi R$, corresponding to the droplet circumference with radius R. The wave motion is sustained by the force generated by the active stress due to gel density in front of (ρ^{front}) and behind (ρ^{behind}) the wave, assembling at a rate k_p. See Note S3 of the Supplemental Material [38] for details. (f) Bifurcation diagram showing wave velocity V_w vs characteristic velocity v_{cv}. (g) Self-consistent equation [Eq. (7)] determining the multipolar wave velocity $V_w^{n\text{-polar}}$ at the intersection of the gray line ($y = V_w^{n\text{-polar}}/v_{cv}$) and the colored lines ($y = g(V_w^{n\text{-polar}})$, $n = 1$ for monopolar in blue; $n = 2$ for bipolar in red; $n = 3$ for tripolar in green; and $n = 4$ for quadrupolar in purple). Scale bars represent 2.

determines the wave-number-dependent revolving wave velocity, we developed a mathematical model [Fig. 4(e); Note S3 of the Supplemental Material; Fig. S16 of the Supplemental Material [38]). We consider a force-balance equation describing the wave motion along one-dimensional periodic domain, $0 < x < 2\pi R$, corresponding to the droplet periphery. The model assumes that (1) revolving wave motion is driven by the active stress around the wave-tip region, (2) the active stress is induced by the newly assembled gels near the droplet periphery, and (3) the gel density gradient between in front of and behind the wave determines the force magnitude. This simple model yields two distinct scenarios:

(1) Unstable revolving wave: The wave moves too slowly to sustain the gel density gradient, resulting in a uniform gel density across the domain $0 < x < 2\pi R$, corresponding to a ring-shaped wave. (2) Stable revolving wave: The wave moves quickly enough to sustain the density gradient, leading to a steady state with a constant revolving velocity V_w. Indeed, the solution of the force-balance equation of revolving wave motion shows a transition from unstable (ring) to stable state (revolving) by increasing the characteristic velocity v_{cv} (proportional to contractility ζ) through a pitchfork bifurcation [Fig. 4(f); Note S3 of the Supplemental Material [38]]. We confirmed the contractility-dependent transition from unstable to stable revolving waves in numerical simulations (Fig. S17 of the Supplemental Material [38]). We extended this model to multipolar waves (Note S3 of the Supplemental Material [38]), leading to the self-consistent equation for the wave velocity of n-polar waves, $V_w^{n\text{-polar}}$:

$$\frac{V_w^{n\text{-polar}}}{v_{cv}} = \exp\left[-\frac{l_w}{V_w^{n\text{-polar}}\tau_d}\right] - \exp\left[-\frac{(2\pi R/n) - l_w}{V_w^{n\text{-polar}}\tau_d}\right], \tag{7}$$

where n is the wave number, $v_{cv} = \zeta\rho_0/(2l_w\gamma)$ is the characteristic velocity, l_w is the wave width, $\rho_0 = k_p/k_d$, and $\tau_d = 1/k_d$. For convenience, we rewrite the self-consistent equation [Eq. (7)] as $V_w^{n\text{-polar}}/v_{cv} = g(V_w^{n\text{-polar}})$, where $g(V_w^{n\text{-polar}}) \equiv \exp[-l_w/(V_w^{n\text{-polar}}\tau_d)] - \exp[-(2\pi R/n - l_w)/(V_w^{n\text{-polar}}\tau_d)]$, such that the solutions correspond to the intersections of $y = g(V_w^{n\text{-polar}})$ with the line $y = V_w^{n\text{-polar}}/v_{cv}$ as a function of V_w using $v_{cv} = 0.025$, $l_w = 1$, $k_d = 0.001$, and $R = 4$. Notably, the stable revolving wave velocity decreases as the wave number increases [Fig. 4(g)], consistent with the trend in the angular velocity of multipolar revolving waves observed in the simulation [Fig. 4(d)]. This theoretical analysis indicates that the wave-number-dependent revolving wave velocity is determined by the balance between gel assembly and force generation in confinement.

III. DISCUSSION

While reaction-diffusion waves have been widely studied to describe adherent cell motility [6,7,53], how the force propagation of contractile waves regulates morphological change and migration remains elusive. We developed a minimal numerical model of cell-like morphodynamics by adopting active gel theory enclosed inside deformable interfaces described by a phase-field model. The stronger interface-gel coupling triggered droplet motility, capturing the observations in living cells and cell-extract droplets in which actin-lipid membrane/interface interaction is essential to trigger spontaneous migration [10,49]. Experimental studies revealed that single cells and cell-extract droplets can migrate under quasi-2D confinement driven by frictional forces between substrates and actin flows [8–10,12,13,45,50,54], whereas how the interplay between wave contraction and shape deformation enables their rich morphodynamics remains unclear. Our results suggest that various morphologies and motility may emerge through a temporal coupling of wave contraction and shape deformation, showing nonmotile, revolving, and motile active gel droplets, which are reminiscent of morphodynamics of living cells and cell-extract droplets accompanied by contractile actomyosin waves [8–10].

It is worth noting that the key parameter explored in this study, the interface-gel coupling strength β, is a coarse-grained phenomenological parameter that captures the collective effects of multiple microscopic processes governing actin-membrane interactions. Consequently, it cannot be uniquely assigned to a single experimentally measurable physical quantity. Nevertheless, we emphasize that the relative values of β between different dynamical states provide experimentally testable predictions for the transitions between wave, revolving, and motile states. Specifically, our simulations predict that $\beta \sim 40$ marks the transition to persistent motility, whereas $\beta < 10-30$ results in nonmotile or revolving states. Assuming that β scales approximately with the effective actin-membrane coupling strength, the ratio $\beta_{\text{nonmotile}}/\beta_{\text{motile}} \sim c_{\text{nonmotile}}/c_{\text{motile}} \sim 0.4-0.75$ provides a quantitative prediction for the relative concentrations ($c_{\text{nonmotile}}/c_{\text{motile}}$) of actin-binding lipids (e.g., PIP_2) or actin-membrane linkers (e.g., His-VCA bound to a fixed concentration of DOGS-NTA lipids) required to induce the transition. Interestingly, previous experimental observations are consistent with this interpretation. It was reported that persistent migration emerged only when the fraction of PIP_2 exceeded ~14% [10]. Similarly, with a fixed lipid composition, increasing the concentration of membrane-bound His-VCA to approximately 10 nM was sufficient to induce migration [10], whereas lower concentrations produced symmetry breaking of an actomyosin cluster without droplet motility [43]. Although β remains a phenomenological parameter, these observations suggest that it captures the effective strength of actin-interface coupling that governs transitions between dynamical states. Important directions for future research include a detailed quantitative comparison between the predicted transition thresholds and experimental measurements, as well as further refinement of the current coarse-grained phenomenological model toward a more physically grounded formulation.

Additionally, we discuss the physical interpretation and estimation of the Péclet number ($\text{Pe} = Ul/D$), which represents the ratio of advective transport to diffusion, to relate the model to experimental actomyosin systems. We provide estimates of Pe based on experimentally measured quantities in systems exhibiting contractile actomyosin waves. In cell-extract droplets with $R \sim 100\,\mu\text{m}$, using the speed of contractile actomyosin waves $U \sim 45\,\mu\text{m/min}$ and typical wave width $l \sim 10\,\mu\text{m}$ [10,43,44], with effective diffusion coefficient $D \sim 0.1\,\mu\text{m}^2/\text{s}$ [21,55–57] (Note S1 of the Supplemental Material [38]), we estimate $\text{Pe} \sim 72$. In living cells with $R \sim 10\,\mu\text{m}$, using the corresponding values of wave speed $U \sim 100\,\mu\text{m/min}$ and wave width $l \sim 1\,\mu\text{m}$ [8,50], with effective diffusion coefficient $D \sim 0.1\,\mu\text{m}^2/\text{s}$ (Note S1 of the Supplemental Material [38]), we estimate $\text{Pe} \sim 16$. Thus, the Péclet numbers in both cell-extract droplets and living cells are comparable to the regime of $20 < \text{Pe} < 50$ explored in this study. An exciting future direction will be to explore how distinct dynamical states can be controlled through modulation of the Péclet number and actin-interface coupling strength in living and synthetic cell systems.

An intriguing morphodynamics of active gels was observed: revolving waves with well-defined symmetry modes.

This indicates that a passive deformable interface is not just deformed by active stresses, while it may impact the self-organization of active gels confined within the interface. While several experimental studies have observed revolving wavelike behaviors in living cells and cell-extract droplets (Zebrafish progenitor cells [8,50], *Xenopus* blastomeres [58], fish parasites [59], and cell-extract droplets [10,44]), to our knowledge, so far lacking a physical framework to understand the intimate relationship between contractile waves and shape deformation. Our numerical model offers a minimal framework to guide how to design experimental systems and control distinct morphological modes in living and synthetic systems. It is worth noting that the revolving waves in our system originate from contractile forces of active gels, distinguishing them from previously reported systems where rotational waves are driven by protrusive forces arising from active gel polymerization [18,24].

Importantly, we demonstrate that time-dependent geometrical confinement acts as an external driving frequency, entraining revolving waves into a mode-locked oscillatory state through temporal coupling between wave contraction and droplet shape deformation. It should be noted that the motile droplet was unconfined, whereas the confined droplet was not allowed to undergo translational motion. An interesting question is what would occur if a translationally motile droplet encountered a rotating confinement: Would mode locking suppress translational migration? In such a scenario, we observed that the migratory state transitioned toward a revolving wave state, in which migration was arrested and the system became synchronized with the imposed rotational dynamics (Movie S13 of the Supplemental Material [38]). Although rotating confinement represents an extreme example of mode locking, periodic dynamics are ubiquitous in living cellular environments. Oscillatory mechanical stresses, such as those associated with heartbeat and breathing [60], may serve as external cues capable of inducing mode locking in living cells exhibiting contractile actomyosin waves, potentially leading to spatial arrest within specific regions. Thus, contractile actomyosin waves may enable living cells and cell-extract droplets to sense and adapt to dynamically changing geometrical environments. Exploring such behaviors will require extending the present model to time-dependent open confinement and combining it with precisely controlled, *in vivo*-mimetic experimental platforms. To experimentally test this, time-varying potential walls could be designed by optical tweezers [61,62] or magnetic fluids [63,64]. While adherent living cells [65] and cytoskeletal motility assays [66] are known to respond to environmental periodic strains, it will be an important future direction to develop time-varying geometry for nonadherent cells and cell-extract droplet systems. Elucidating these principles paves the way to coordinate spatiotemporal events in living matter—from living cells to reconstituted droplets—and may inform the engineering of soft, adaptive, lifelike robotic systems [67].

IV. CONCLUSIONS

We have introduced a minimal numerical model that demonstrates how contraction waves reshape deformable droplets. The model reveals a feedback mechanism between wave dynamics and a deformable interface, which gives rise to cell-like motility and rotationally symmetric waveforms. By imposing rotating confinement, we further show that the mode of contraction waves can be selectively controlled. Together, these results provide a dynamical-systems perspective on the coupling between contraction waves and shape deformation that governs the morphodynamics of active gel droplets as actively driven fluid oscillators under confinement, a general principle relevant to nonequilibrium active systems ranging from living and synthetic cells to biomimetic robotics.

V. METHODS

A. Active gel dynamics inside a phase-field droplet

A continuum hydrodynamic description of a 2D active gel confined inside a phase-field droplet domain is given by Eqs. (4)–(6). The viscous stress, $\boldsymbol{\sigma}_{\rm vis}$, in Eq. (1) is given by the dissipative part of the viscous fluids [21]:

$$\boldsymbol{\sigma}_{\rm vis} = \eta[\nabla\mathbf{v} + (\nabla\mathbf{v})^T] + \eta_{\rm b}(\nabla\cdot\mathbf{v})\mathbf{I}, \tag{8}$$

where η and $\eta_{\rm b}$ are dynamic and bulk viscosities, respectively, and $\mathbf{I}$ is the identity matrix. In the nondimensionalized form [Eq. (4)], $\lambda \equiv 1 + \eta/\eta_{\rm b}$ was introduced, which was assumed to be $\lambda = 1/3$ to simplify the momentum balance equation [21,47].

In the nondimensionalized mass conservation equation in Eq. (5), the no-flux boundary condition on actomyosin gel was imposed by an effective energy, $E(\rho,\phi) = \iint \mathrm{d}\mathbf{r}\{(\rho^2+\delta)[(1-\phi)^2+\delta]\}^{1/2}$, which is an addition to the chemical potential of the active gel, and δ was introduced to avoid singularities [21,26]. The explicit form of the functional derivative in Eq. (5) is $\delta E/\delta\rho = \rho\{(\rho^2+\delta)^{-1}[(1-\phi)^2+\delta)]\}^{1/2}$.

In the phase-field model in Eq. (6), the second term with $V'(\phi)$ is the derivative of the double-well potential $V(\phi) = \phi(\phi-1)[\phi - 1/2 - \alpha_0(V_{\rm drop}/V_{\rm tar} - 1)]$, where the fixed points describe the outside ($\phi = 0$) and inside of the droplet ($\phi = 1$) [21,26]. The term $\alpha_0(V_{\rm drop}/V_{\rm tar} - 1)$ describes the conservation of droplet volume $V_{\rm drop} = \iint \mathrm{d}\mathbf{r}\phi$ toward a target volume $V_{\rm tar}$, which corresponds to the initial droplet volume. We used $V_{\rm drop} = \iint \mathrm{d}\mathbf{r}\phi^2(3-2\phi)$ in this study for more accurate calculation [21,68]. The parameter α_0 characterizes the stiffness of this constraint [16]. The other terms were explained in the main text.

B. Active gel droplets under rotating confinement

For the implementation of rotating confinement, we applied a potential wall by adding an external field term $-\Gamma_{\rm wall}g_{\rm mask}(\mathbf{r})\phi$ in the right-hand side of phase-field equation in Eq. (6) with a constant $\Gamma_{\rm wall} = 100$. The mask function $g_{\rm mask}(\mathbf{r})$ was prepared by assigning specific geometry where $g_{\rm mask}(\mathbf{r}) = 0$ and $g_{\rm mask}(\mathbf{r}) = 1$ describe the inside and outside of confinement, respectively. Mode $n = 1$ is a circle with radius 4.8 off-centered by $x = 0.8$. Mode $n = 2$ is an ellipse with major and minor axis lengths of 5.6 and 4.2, respectively. Mode $n = 3$ is a combination of three ellipses rotated by 120° with major and minor axis lengths of 6.4 and 3.2, respectively. Mode $n = 4$ is a combination of four circles with radius 8.3,

with their center separated by 4.2. Time-dependent rotation of mask function was applied at each time step with angular velocity $\omega_{\rm rot}$.

C. Numerical simulations

The nondimensionalized Eqs. (4)–(6) were numerically solved. The numerical simulations were performed using a custom MATLAB code implementing a semi-implicit spectral method on a 128×128 lattice with periodic boundary conditions. The grid spacing and time step were set to $dx = 0.125$ and $dt = 0.0007$, respectively. At each time step, the velocity field was computed using Eq. (4), and the gel density and phase field were updated using Eqs. (5) and (6). The area of assembly rate enhanced region near the droplet interface was computed at each time step with thresholds $\nabla^2\phi < -0.01$ and $\phi > 0.95$ (Fig. S3 of the Supplemental Material [38]). Each single-droplet simulation was run for 30 000 time steps and data were recorded every 200 steps, yielding 150 frame sets per simulation, respectively. These data were used to analyze the time courses of droplet motion and shape changes, as well as to generate the movies.

D. Contour analysis of the droplet shape deformation

The contour position of the droplet phase was extracted from pixel values in the phase-field, binarized by a threshold of $\phi > 0.99$. The center of mass of the droplet, $\mathbf{r}_c = N^{-1}\Sigma\mathbf{r}_i$, was calculated from the position of the membrane, $\mathbf{r}_i = (x_i, y_i),\ i = 1 \cdots N$. The origin of the polar coordinate was then centered at the center of mass of the droplet by subtracting the center of mass of the contour position from each position of the membrane as $\mathbf{r}_i - \mathbf{r}_c$. To calculate the aspect ratio of a droplet $\alpha = R_{\rm max}/R_{\rm min}$, the major axis length $R_{\rm max}$ and minor axis length $R_{\rm min}$ of a droplet were determined by fitting an ellipse to the contour position. We computed radial length $R(\theta, t)$ by converting $\mathbf{r}_i = (x_i, y_i)$ in polar coordinates. The amplitude of deformation $u(\theta, t) = R(\theta, t) - \langle R(\theta, t)\rangle_\theta$ was calculated in polar coordinates centered at droplet centroid, where $\langle R(\theta, t)\rangle_\theta$ is the mean radius averaged over θ at time t. The time course of centroid speed and MSD [Fig. 2(c)], polarity [Fig. 2(k)], aspect ratio (Fig. S12 of the Supplemental Material [38]), and equal-angle autocorrelation of amplitude [Fig. 2(g)], were shown for the droplets in the vicinity of the phase boundary with different Pe and β for each motile and nonmotile condition.

E. Polarity parameter analysis

We quantified the active gel distribution using the gel polarity parameter P. First, the center of mass of the droplet, $\mathbf{r}_c = N^{-1}\Sigma\mathbf{r}_i$, is calculated from droplet contour positions, $\mathbf{r}_i = (x_i, y_i),\ i = 1 \cdots N$. The local gel density was measured at each interfacial position, $\rho(\mathbf{r}_i)$. Then, the center of mass of the gel distribution, $\mathbf{r}_{\rm gel}$, was calculated as the gel density-weighted contour position, $\mathbf{r}_{\rm gel} = \Sigma\mathbf{r}_i\rho(\mathbf{r}_i)/\Sigma\rho(\mathbf{r}_i)$. Finally, we defined the gel polarity, $P \equiv |\mathbf{r}_{\rm gel} - \mathbf{r}_c|/R$, as the deviation of the gel distribution from the center of mass of the droplet, normalized by the initial droplet radius R. The polarity parameter approaches $P \to 1$ for polarized gel distribution, while it approaches $P \to 0$ for nonpolarized gel distribution. The polarity vector was defined as $\vec{p}(t) = (\mathbf{r}_{\rm gel} - \mathbf{r}_c)/|\mathbf{r}_{\rm gel} - \mathbf{r}_c|$ (Fig. 2).

F. Shape analysis of the active gels

The same analysis protocol as the droplet shape was applied to quantify the shape of active gels inside droplets. The contour position of the gel was extracted from pixel values in the gel density, binarized by a threshold of $\rho > 1.5$. Converting the peripheral positions into polar coordinate, the deformation amplitude of the gel, $u_{\rm gel}(\theta, t)$, was used to calculate equal-time autocorrelation of gel deformation, $C_{tt}(\Delta\theta) \equiv \langle u(\theta, t)_{\rm gel} u_{\rm gel}(\theta + \Delta\theta, t)\rangle_{\theta,t}/\langle u_{\rm gel}(\theta, t)^2\rangle_{\theta,t}$, which was used to estimate the extent to which the shape of the gel was retained (Fig. S14 of the Supplemental Material [38]). The maximum value of the shape correlation, $C_{tt}^{\rm max}$, was extracted from the largest peak of the $C_{tt}(\Delta\theta) - \Delta\theta$ curve, and values with $C_{tt}^{\rm max} < 0$ were set to 0. In order to avoid extracting the values originating from the circular shape of the high-density region in the droplet center, $C_{tt}^{\rm max}$ were extracted within the range at $\Delta\theta > 45^\circ$ for the confinement modes $n = 2,\ 3,\ 4$, and at $\Delta\theta < 135^\circ$ for $n = 3,\ 4$. The results were assessed by the time-lapse movies to ensure there are no wave-mode-associated peaks outside this range. We confirmed that the angle at which $C_{tt}(\Delta\theta = \Delta\theta_{\rm max}) = C_{tt}^{\rm max}$ reflects the modes of each revolving wave, where $\Delta\theta_{\rm max} = 180^\circ$ for bipolar, $\Delta\theta_{\rm max} = 120^\circ$ for tripolar, and $\Delta\theta_{\rm max} = 90^\circ$ for quadrupolar waves. We found $\Delta\theta_{\rm max} = 19^\circ$ for monopolar waves because the center of mass resides outside the gel. This does not affect to distinguish revolving waves from ring-shaped waves since $C_{tt}^{\rm max}$ represents the extent to which shape is retained in a time- and angle-averaged manner, in which the periodic contraction of ring-shaped waves reports small values, while the retained shape of monopolar waves reports large values of autocorrelation.

ACKNOWLEDGMENTS

We thank T. Hiraiwa for insightful discussions and helpful comments on the manuscript. The authors acknowledge funding/grant support from National Science and Technology Council, Taiwan, Grant No. NSTC114-2112-M-001–066-MY3 (to R.S.), and JST PRESTO, Japan, Grant No. JPMJPR2534 (to R.S.). R.S. acknowledges support from the Institute of Physics at Academia Sinica startup funding.

R.S. designed and conceptualized the research. R.S. developed the theoretical model and numerical simulations. R.S. and A.A. performed numerical simulations and analyzed the data. A.A. performed the linear stability analysis. R.S. drafted the manuscript. R.S. and A.A. edited the manuscript.

The authors declare no competing interests.

DATA AVAILABILITY

All study data are included in the article and/or Supplemental Material [38]. Code supporting the findings of this manuscript has been deposited in Ref. [69] and is publicly available as of the date of publication.

[1] S. Sawai, P. A. Thomason, and E. C. Cox, An autoregulatory circuit for long-range self-organization in *Dictyostelium* cell populations, Nature (London) **433**, 323 (2005).

[2] K. Aoki, Y. Kondo, H. Naoki, T. Hiratsuka, R. E. Itoh, and M. Matsuda, Propagating wave of ERK activation orients collective cell migration, Dev. Cell **43**, 305 (2017).

[3] M. T. Abreu-Blanco, J. M. Verboon, and S. M. Parkhurst, Coordination of Rho family GTPase activities to orchestrate cytoskeleton responses during cell wound repair, Curr. Biol. **24**, 144 (2014).

[4] W. M. Bement, M. Leda, A. M. Moe, A. M. Kita, M. E. Larson, A. E. Golding, C. Pfeuti, K.-C. Su, A. L. Miller, A. B. Goryachev, and G. von Dassow, Activator–inhibitor coupling between Rho signalling and actin assembly makes the cell cortex an excitable medium, Nat. Cell Biol. **17**, 1471 (2015).

[5] E. L. Barnhart, J. Allard, S. S. Lou, J. A. Theriot, and A. Mogilner, Adhesion-dependent wave generation in crawling cells, Curr. Biol. **27**, 27 (2017).

[6] G. Danuser, J. Allard, and A. Mogilner, Mathematical modeling of eukaryotic cell migration: Insights beyond experiments, Annu. Rev. Cell Dev. Biol. **29**, 501 (2013).

[7] D. L. Bodor, W. Pönisch, R. G. Endres, and E. K. Paluch, Of cell shapes and motion: The physical basis of animal cell migration, Dev. Cell **52**, 550 (2020).

[8] V. Ruprecht, S. Wieser, A. Callan-Jones, M. Smutny, H. Morita, K. Sako, V. Barone, M. Ritsch-Marte, M. Sixt, R. Voituriez, and C. P. Heisenberg, Cortical contractility triggers a stochastic switch to fast amoeboid cell motility, Cell **160**, 673 (2015).

[9] A. Reversat, F. Gaertner, J. Merrin, J. Stopp, S. Tasciyan, J. Aguilera, I. de Vries, R. Hauschild, M. Hons, M. Piel, A. Callan-Jones, R. Voituriez, and M. Sixt, Cellular locomotion using environmental topography, Nature (London) **582**, 582 (2020).

[10] R. Sakamoto, Z. Izri, Y. Shimamoto, M. Miyazaki, and Y. T. Maeda, Geometric trade-off between contractile force and viscous drag determines the actomyosin-based motility of a cell-sized droplet, Proc. Natl. Acad. Sci. USA **119**, e2121147119 (2022).

[11] Y. Miao, S. Bhattacharya, T. Banerjee, B. Abubaker-Sharif, Y. Long, T. Inoue, P. A. Iglesias, and P. N. Devreotes, Wave patterns organize cellular protrusions and control cortical dynamics, Mol. Syst. Biol. **15**, e8585 (2019).

[12] M. Bergert, A. Erzberger, R. A. Desai, I. M. Aspalter, A. C. Oates, G. Charras, G. Salbreux, and E. K. Paluch, Force transmission during adhesion-independent migration, Nat. Cell Biol. **17**, 524 (2015).

[13] E. K. Paluch, I. M. Aspalter, and M. Sixt, Focal adhesion–independent cell migration, Annu. Rev. Cell Dev. Biol. **32**, 469 (2016).

[14] J. Prost, F. Jülicher, and J.-F. Joanny, Active gel physics, Nat. Phys. **11**, 111 (2015).

[15] D. Shao, W. J. Rappel, and H. Levine, Computational model for cell morphodynamics, Phys. Rev. Lett. **105**, 108104 (2010).

[16] F. Ziebert, S. Swaminathan, and I. S. Aranson, Model for self-polarization and motility of keratocyte fragments, J. R. Soc. Interface **9**, 1084 (2012).

[17] B. A. Camley, Y. Zhao, B. Li, H. Levine, and W.-J. Rappel, Periodic migration in a physical model of cells on micropatterns, Phys. Rev. Lett. **111**, 158102 (2013).

[18] A. Dreher, I. S. Aranson, and K. Kruse, Spiral actin-polymerization waves can generate amoeboidal cell crawling, New J. Phys. **16**, 055007 (2014).

[19] B. A. Camley, Y. Zhang, Y. Zhao, B. Li, E. Ben-Jacob, H. Levine, and W.-J. Rappel, Polarity mechanisms such as contact inhibition of locomotion regulate persistent rotational motion of mammalian cells on micropatterns, Proc. Natl. Acad. Sci. USA **111**, 14770 (2014).

[20] F. Ziebert and I. S. Aranson, Computational approaches to substrate-based cell motility, npj Comput. Mater. **2**, 16019 (2016).

[21] T. Le Goff, B. Liebchen, and D. Marenduzzo, Actomyosin contraction induces in-bulk motility of cells and droplets, Biophys. J. **119**, 1025 (2020).

[22] J. Löber, F. Ziebert, and I. S. Aranson, Collisions of deformable cells lead to collective migration, Sci. Rep. **5**, 9172 (2015).

[23] J. Löber, F. Ziebert, and I. S. Aranson, Modeling crawling cell movement on soft engineered substrates, Soft Matter **10**, 1365 (2014).

[24] C. Reeves, B. Winkler, F. Ziebert, and I. S. Aranson, Rotating lamellipodium waves in polarizing cells, Commun. Phys. **1**, 73 (2018).

[25] N. Ecker and K. Kruse, Excitable actin dynamics and amoeboid cell migration, PLoS One **16**, e0246311 (2021).

[26] R. Sakamoto, M. Miyazaki, and Y. T. Maeda, State transitions of a confined actomyosin system controlled through contractility and polymerization rate, Phys. Rev. Res. **5**, 013208 (2023).

[27] A. Negi, R. Sakamoto, R. Ienaga, M. Miyazaki, and Y. T. Maeda, Myosin-driven advection and actin reorganization control the geometry of confined actomyosin gel, Nano Lett. **25**, 17979 (2025).

[28] T. Guyomar, L. Lu, T. Hiraiwa, and D. Riveline, Asymmetric cortical mechanics shape epithelial cell geometry in organoids, Phys. Rev. Res. (2026).

[29] G. Salbreux, J. Prost, and J. F. Joanny, Hydrodynamics of cellular cortical flows and the formation of contractile rings, Phys. Rev. Lett. **103**, 058102 (2009).

[30] J. S. Bois, F. Jülicher, and S. W. Grill, Pattern formation in active fluids, Phys. Rev. Lett. **106**, 028103 (2011).

[31] K. V. Kumar, J. S. Bois, F. Jülicher, and S. W. Grill, Pulsatory patterns in active fluids, Phys. Rev. Lett. **112**, 208101 (2014).

[32] T. Moore, S. K. Wu, M. Michael, A. S. Yap, G. A. Gomez, and Z. Neufeld, Self-organizing actomyosin patterns on the cell cortex at epithelial cell-cell junctions, Biophys. J. **107**, 2652 (2014).

[33] K. Kruse, J. F. Joanny, F. Jülicher, J. Prost, and K. Sekimoto, Generic theory of active polar gels: A paradigm for cytoskeletal dynamics, Eur. Phys. J. E **16**, 5 (2005).

[34] E. Hannezo, B. Dong, P. Recho, J.-F. Joanny, and S. Hayashi, Cortical instability drives periodic supracellular actin pattern formation in epithelial tubes, Proc. Natl. Acad. Sci. USA **112**, 8620 (2015).

[35] N. Levernier and K. Kruse, Spontaneous formation of chaotic protrusions in a polymerizing active gel layer, New J. Phys. **22**, 013003 (2020).

[36] S. Stam, J. Alberts, M. L. Gardel, and E. Munro, Isoforms confer characteristic force generation and mechanosensation by myosin II filaments, Biophys. J. **108**, 1997 (2015).

[37] M. Kovács, F. Wang, A. Hu, Y. Zhang, and J. R. Sellers, Functional divergence of human cytoplasmic myosin II, J. Biol. Chem. **278**, 38132 (2003).

[38] See Supplemental Material at http://link.aps.org/supplemental/10.1103/cnn8-lrdx for Notes S1–S3, Figs. S1–S17, and Movies S1–S13.

[39] J. Alvarado, M. Sheinman, A. Sharma, F. C. MacKintosh, and G. H. Koenderink, Force percolation of contractile active gels, Soft Matter **13**, 5624 (2017).

[40] J. Alvarado, M. Sheinman, A. Sharma, F. C. MacKintosh, and G. H. Koenderink, Molecular motors robustly drive active gels to a critically connected state, Nat. Phys. **9**, 591 (2013).

[41] I. Linsmeier, S. Banerjee, P. W. Oakes, W. Jung, T. Kim, and M. P. Murrell, Disordered actomyosin networks are sufficient to produce cooperative and telescopic contractility, Nat. Commun. **7**, 12615 (2016).

[42] C. M. Field, M. Wühr, G. A. Anderson, H. Y. Kueh, D. Strickland, and T. J. Mitchison, Actin behavior in bulk cytoplasm is cell cycle regulated in early vertebrate embryos, J. Cell Sci. **124**, 2086 (2011).

[43] R. Sakamoto, M. Tanabe, T. Hiraiwa, K. Suzuki, S. Ishiwata, Y. T. Maeda, and M. Miyazaki, Tug-of-war between actomyosin-driven antagonistic forces determines the positioning symmetry in cell-sized confinement, Nat. Commun. **11**, 3063 (2020).

[44] A. Krishna, M. Savinov, N. Ierushalmi, A. Mogilner, and K. Keren, Size-dependent transition from steady contraction to waves in actomyosin networks with turnover, Nat. Phys. **20**, 123 (2024).

[45] J. M. García-Arcos, J. Ziegler, S. Grigolon, L. Reymond, G. Shajepal, C. J. Cattin, A. Lomakin, D. J. Müller, V. Ruprecht, S. Wieser, R. Voituriez, and M. Piel, Rigidity percolation and active advection synergize in the actomyosin cortex to drive amoeboid cell motility, Dev. Cell **59**, 2990 (2024).

[46] J. F. Joanny, K. Kruse, J. Prost, and S. Ramaswamy, The actin cortex as an active wetting layer, Eur. Phys. J. E **36**, 52 (2013).

[47] G. K. Batchelor, *An Introduction to Fluid Dynamics*, Cambridge Mathematical Library (Cambridge University Press, Cambridge, 2000).

[48] M. Pinot, V. Steiner, B. Dehapiot, B. K. Yoo, F. Chesnel, L. Blanchoin, C. Kervrann, and Z. Gueroui, Confinement induces actin flow in a meiotic cytoplasm, Proc. Natl. Acad. Sci. USA **109**, 11705 (2012).

[49] A. Bisaria, A. Hayer, D. Garbett, D. Cohen, and T. Meyer, Membrane-proximal F-actin restricts local membrane protrusions and directs cell migration, Science **368**, 1205 (2020).

[50] V. Venturini, F. Pezzano, F. Català Castro, H.-M. Häkkinen, S. Jiménez-Delgado, M. Colomer-Rosell, M. Marro, Q. Tolosa-Ramon, S. Paz-López, M. A. Valverde, J. Weghuber, P. Loza-Alvarez, M. Krieg, S. Wieser, and V. Ruprecht, The nucleus measures shape changes for cellular proprioception to control dynamic cell behavior, Science **370**, eaba2644 (2020).

[51] E. Tjhung, D. Marenduzzo, and M. E. Cates, Spontaneous symmetry breaking in active droplets provides a generic route to motility, Proc. Natl. Acad. Sci. USA **109**, 12381 (2012).

[52] P. Maiuri, J.-F. Rupprecht, S. Wieser, V. Ruprecht, O. Bénichou, N. Carpi, M. Coppey, S. De Beco, N. Gov, C.-P. Heisenberg, C. Lage Crespo, F. Lautenschlaeger, M. Le Berre, A.-M. Lennon-Dumenil, M. Raab, H.-R. Thiam, M. Piel, M. Sixt, and R. Voituriez, Actin flows mediate a universal coupling between cell speed and cell persistence, Cell **161**, 374 (2015).

[53] N. Tamemoto and H. Noguchi, Pattern formation in reaction–diffusion system on membrane with mechanochemical feedback, Sci. Rep. **10**, 19582 (2020).

[54] Y.-J. Liu, M. Le Berre, F. Lautenschlaeger, P. Maiuri, A. Callan-Jones, M. Heuzé, T. Takaki, R. Voituriez, and M. Piel, Confinement and low adhesion induce fast amoeboid migration of slow mesenchymal cells, Cell **160**, 659 (2015).

[55] R. Uehara, G. Goshima, I. Mabuchi, R. D. Vale, J. A. Spudich, and E. R. Griffis, Determinants of myosin II cortical localization during cytokinesis, Curr. Biol. **20**, 1080 (2010).

[56] J. E. Friend, W. A. Sayyad, R. Arasada, C. D. McCormick, J. E. Heuser, and T. D. Pollard, Fission yeast Myo2: Molecular organization and diffusion in the cytoplasm, Cytoskeleton (Hoboken) **75**, 164 (2018).

[57] R. Milo and R. Phillips, *Cell biology by the Numbers* (CRC Press, 2015).

[58] G. T. Charras, M. Coughlin, T. J. Mitchison, and L. Mahadevan, Life and times of a cellular bleb, Biophys. J. **94**, 1836 (2008).

[59] G. Alama-Bermejo, A. S. Holzer, and J. L. Bartholomew, Myxozoan adhesion and virulence: *Ceratonova shasta* on the move, Microorganisms **7**, 397 (2019).

[60] C. Hahn and M. A. Schwartz, Mechanotransduction in vascular physiology and atherogenesis, Nat. Rev. Mol. Cell Biol. **10**, 53 (2009).

[61] A. Ashkin, Optical trapping and manipulation of neutral particles using lasers, Proc. Natl. Acad. Sci. USA **94**, 4853 (1997).

[62] J. Guck, R. Ananthakrishnan, H. Mahmood, T. J. Moon, C. C. Cunningham, and J. Käs, The optical stretcher: A novel laser tool to micromanipulate cells, Biophys. J. **81**, 767 (2001).

[63] W. Zhao, R. Cheng, J. R. Miller, and L. Mao, Label-free microfluidic manipulation of particles and cells in magnetic liquids, Adv. Funct. Mater. **26**, 3916 (2016).

[64] K. Beppu and J. V. I. Timonen, Magnetically controlled bacterial turbulence, Commun. Phys. **7**, 216 (2024).

[65] A. Livne, E. Bouchbinder, and B. Geiger, Cell reorientation under cyclic stretching, Nat. Commun. **5**, 3938 (2014).

[66] D. Inoue, T. Nitta, A. M. R. Kabir, K. Sada, J. P. Gong, A. Konagaya, and A. Kakugo, Sensing surface mechanical deformation using active probes driven by motor proteins, Nat. Commun. **7**, 12557 (2016).

[67] O. E. Shklyaev and A. C. Balazs, Interlinking spatial dimensions and kinetic processes in dissipative materials to create synthetic systems with lifelike functionality, Nat. Nanotechnol. **19**, 146 (2024).

[68] M. Nonomura, Study on multicellular systems using a phase field model, PLoS One **7**, e33501 (2012).

[69] R. Sakamoto, activefluid_phasefield_coupled_waverotmig_sakamoto_ver1.0 (Version 1.0) [Computer software], Zenodo, 2026, https://doi.org/10.5281/zenodo.21967605.